ADVANCED ENERGY & SUSTAINABILITY RESEARCH
Open Access
www.advenergysustres.com

Intercalation of Ammonium Cationic Ligands Enabled Grain Surface Passivation in Sequential-Deposited Perovskite Solar Cells

*Hock Beng Lee, Neetesh Kumar, Sinyoung Cho, Seungyeon Hong, Hyun Hwi Lee, Hyo Jung Kim, Jong-Soo Lee, and Jae-Wook Kang**

Solution-processed formamidinium lead iodide ($FAPbI_3$) perovskite typically contains a high number of ionic defects that are intrinsically formed during film formation. To reduce the defects, postsynthetic surface passivation treatment is widely practiced. However, the practicality of the surface passivation approach is limited by the poor coverage and incomplete adsorption of passivators into the defective sites. Unprecedentedly, the use of 4-(trifluoromethyl)benzylammonium iodide (CF_3BZAI) is demonstrated as a novel passivator additive for sequentially deposited perovskite films. Due to its unique molecular structure and trifluoromethyl (–CF_3) moiety, CF_3BZAI is expected to have enhanced adsorption with defect sites during the film formation. Owing to grain surface passivation, the CF_3BZAI-intercalated $FAPbI_3$ (target) film has enhanced morphology and crystallinity as well as significantly fewer defects than the normal $FAPbI_3$ film. Interestingly, the intercalation of CF_3BZAI passivators does not lead to the formation of a low-dimensional perovskite phase in $FAPbI_3$ films. The best perovskite solar cell (PSC) device based on the target film achieves a maximum efficiency of ≈22.4%, which is much higher than the efficiency (≈20.7%) of the normal device. CF_3BZAI-assisted grain surface passivation is a facile yet effective strategy to enhance the performance and stability of $FAPbI_3$-based PSCs.

1. Introduction

Solution-processed metal halide perovskites, particularly formamidinium lead iodide ($FAPbI_3$), has been widely used for photovoltaic applications because of their outstanding optoelectronic properties, including a near-optimal Goldschmidt tolerance factor, low exciton binding energy (BE), high carrier diffusion length and mobility, high optical absorption efficient, and tunable bandgap.[1,2] However, the excellent optoelectronic properties of $FAPbI_3$ perovskite are severely undermined by its polymorphic crystal structure and poor environmental stability, hindering the commercialization potential of $FAPbI_3$-based perovskite solar cells (PSCs).[3] As is commonly known, solution-processed $FAPbI_3$ films typically contain a high density (10^{15}–10^{16} cm^3) of halide vacancies, Pb interstitials, and point defects that exist predominantly on the film surface and grain boundaries.[4,5] When left unattended, these intrinsic defects can turn into undesirable recombination sites that trap charge carriers or vulnerable sites for the permeation of moisture and oxygen. Moreover, these defects can induce an involuntary α-phase (photoactive) → δ-phase (nonphotoactive) transformation in defect-rich $FAPbI_3$ films at room temperature, further threatening the performance and stability of PSCs.[6]

In this regard, several research strategies including solvent/antisolvent engineering,[7,8] additive engineering,[9,10] interfacial modifications,[11,12] alloying and doping,[13,14] and defect passivation[15,16] have been attempted to reduce the defects and improve the structural stability of $FAPbI_3$ films. Among these approaches, grain surface (film surface and grain

H. B. Lee, N. Kumar, J.-W. Kang
Department of Flexible and Printable Electronics
LANL-JBNU Engineering Institute-Korea
Jeonbuk National University
Jeonju 54896, Republic of Korea
E-mail: jwkang@jbnu.ac.kr

The ORCID identification number(s) for the author(s) of this article can be found under https://doi.org/10.1002/aesr.202200128.

DOI: 10.1002/aesr.202200128

S. Cho, J.-S. Lee
Department of Energy Science and Engineering
DGIST
Daegu 42988, Republic of Korea

S. Hong, H. J. Kim
Department of Organic Material Science and Engineering
School of Chemical Engineering
Pusan National University
Busan 46241, Republic of Korea

H. H. Lee
Pohang Accelerator Laboratory
POSTECH
Pohang 37673, Republic of Korea

boundaries) passivation is the most promising strategy to increase the carrier diffusion length and reduce the defect trap states of perovskite films, given that the grain surfaces typically exhibit a trap density several orders of magnitude higher than that within the grains.[17,18] The improvement brought by the surface passivation approach is highly dependent on the surface coverage and adsorption efficiency of the passivating agents onto the defect sites of the perovskite film.[19,20] In most of these studies, surface passivators were deposited extrinsically on the readily formed perovskite film via high-speed spin coating. Incomplete adsorption of passivating agents during spin coating may lead to insufficient defect passivation and limited improvement of the device performance and stability. To improve the passivator adsorption, it is better to incorporate the passivating agent as an additive into the perovskite precursor solution. This can improve the adsorption and interaction of passivators with the defects on the grain surfaces during the formation of the perovskite film.

For two-step sequential-deposited perovskite films, various precursor additives such as methylammonium chloride,[21] trimesic acid,[22] lead thiocyanate,[23] cesium iodide/bromide,[24] 4-*tert*-butylpyridine,[25] and biguanide hydrochloride[26] have been incorporated as a crystallization agent at the precursor stage. More recently, bulky aliphatic/aromatic ammonium cations such as *n*-butylammonium,[27] *n*-octylammonium,[28] phenethylammonium,[29] 4-chlorobenzamide,[30] 3-bromobenzylammonium,[31] 2-(methylthio)ethylammonium,[32] 4-vinylbenzylammonium,[33] and guanidinium[34] have been used for the surface passivation of perovskite films, all of which have produced highly positive outcomes. In some of these studies, surface passivation with bulky ammonium cations has led to the formation of low-dimensional (2D/quasi-2D) perovskite phases atop the $FAPbI_3$ film.

Herein, for the first time, we demonstrate the two-step sequential deposition of highly crystalline α-$FAPbI_3$ perovskite films using 4-(trifluoromethyl)benzylammonium iodide (CF_3BZAI) as a novel passivator additive. CF_3BZAI is a bulky molecule and its molecular structure constitutes a polar ammonium head group, a unique trifluoromethyl group (–CF_3) moiety, and a benzene ring with a high delocalized electron cloud density, which is beneficial for the electronic properties of the perovskite film. Recent literature elucidates that CF_3-bearing ammonium cations have an enhanced passivator adsorption on surface defective sites at elevated crystallization temperatures compared to common ammonium cations such as butylammonium or phenethylammonium.[17] Similarly, the highly electronegative –CF_3 moiety in CF_3BZA^+ has a high tendency to withdraw electrons from neighboring atoms, leaving the ammonium cation (NH_3^+) with strong electropositivity, thus enhancing the binding with acceptor-type (negatively charged) defects at the grain surfaces of the perovskite films.[31] This enables CF_3BZA^+ to have a stronger perovskite surface–passivator interaction than other ammonium cations, which are only partially adsorbed on the perovskite surface defective sites.

CF_3BZAI has been used as a surface passivator to improve the efficiency and stability of one-step antisolvent processed perovskite films.[15,35,36] Nonetheless, the intercalation of CF_3BZAI in two-step sequential-deposited perovskite films remains unexplored. Our results reveal that the intercalation of CF_3BZAI passivators has greatly enhanced the morphology, grain size, and crystallinity of $FAPbI_3$ films. Additionally, the strong steric repulsion in the benzene ring and –CF_3 moiety of the CF3BZAI passivator improved the surface hydrophobicity of the perovskite film and increased its moisture tolerance. The CF_3BZAI-intercalated perovskite film also exhibited significantly less defect trap states and reduced recombination loss than the pristine film. As a result, the PSC based on the CF_3BZAI-intercalated perovskite film achieved a maximum power conversion efficiency (PCE) of ≈22.4%, which is a remarkable improvement compared to the normal device (PCE ≈20.7%). The environmental stability and operational stability of the PSCs also improved with intercalation of the CF_3BZAI passivator. The improved crystallinity and grain boundary passivation proved to be essential factors to attain the levels of efficiency and stability demonstrated by our two-step fabricated $FAPbI_3$-based PSCs.

2. Results and Discussion

Figure 1a schematically illustrates the full fabrication process of the $FAPbI_3$-based PSCs. α-$FAPbI_3$ perovskite films were prepared using a two-step sequential deposition technique, which commences with the deposition of a PbI_2 film. For the control perovskite film, a FAI:MAI:MACl (90:9:10 mg mL^{-1}) ternary salt solution was used to convert the PbI_2 underlayer into an α-$FAPbI_3$ film. Meanwhile, for the target (CF_3BZAI-intercalated) perovskite film, a FAI:MAI:CF_3BZAI:MACl (90:4.5:4.5:10 mg mL^{-1}) quaternary salt solution was used for $PbI_2 \rightarrow$ α-$FAPbI_3$ conversion by adding an appropriate amount of CF_3BZAI salt. The control and target α-$FAPbI_3$ films were then used as photoabsorbers in PSC devices. X-ray diffraction (XRD) measurements were performed to investigate the structural properties and crystallography of the perovskite films and the results are presented in Figure 1b. Both the control and target perovskite films exhibited prominent diffraction peaks at 2θ positions of ≈14° and ≈28°, corresponding to the α(110) and α(220) planes, respectively. Comparatively, the target film shows a higher degree of crystallinity than the control film, evidenced by the higher intensities of the α(110) and α(220) peaks. The target film showed no sign of new diffraction peaks, indicating that there is no formation of low-dimensional perovskite or impurity phases in the perovskite film following the intercalation of CF_3BZAI.

Additionally, Fourier transform infrared spectroscopy (FTIR) measurements were conducted in the attenuated total reflection (ATR) mode to understand how the intercalation of CF_3BZAI influences the perovskite film growth dynamic. The ATR-FTIR spectra in Figure 1c reveal the characteristic N–H, C=N, and C–H stretching bands in both control and target films, which arises primarily from the FA^+/MA^+ in the host perovskite lattice. The noticeably higher signal intensities of the N–H, C=N, and C–H functional groups in the target film is attributable to presence of the intercalated CF_3BZA^+ in the perovskite framework. No peak shifts were observed, indicating that the intercalation of CF_3BZAI has negligible impact on the structural and hybridization state of the host perovskite. This may enable the formation of a more stoichiometric film with lesser organic cation vacancies or lattice defects. Figure 1d displays the UV–vis absorption and steady-state PL spectra of the control and target films. Although both perovskite films exhibited rather similar UV–vis absorption profiles, the target film demonstrated a significantly higher PL intensity than the control film. This phenomenon

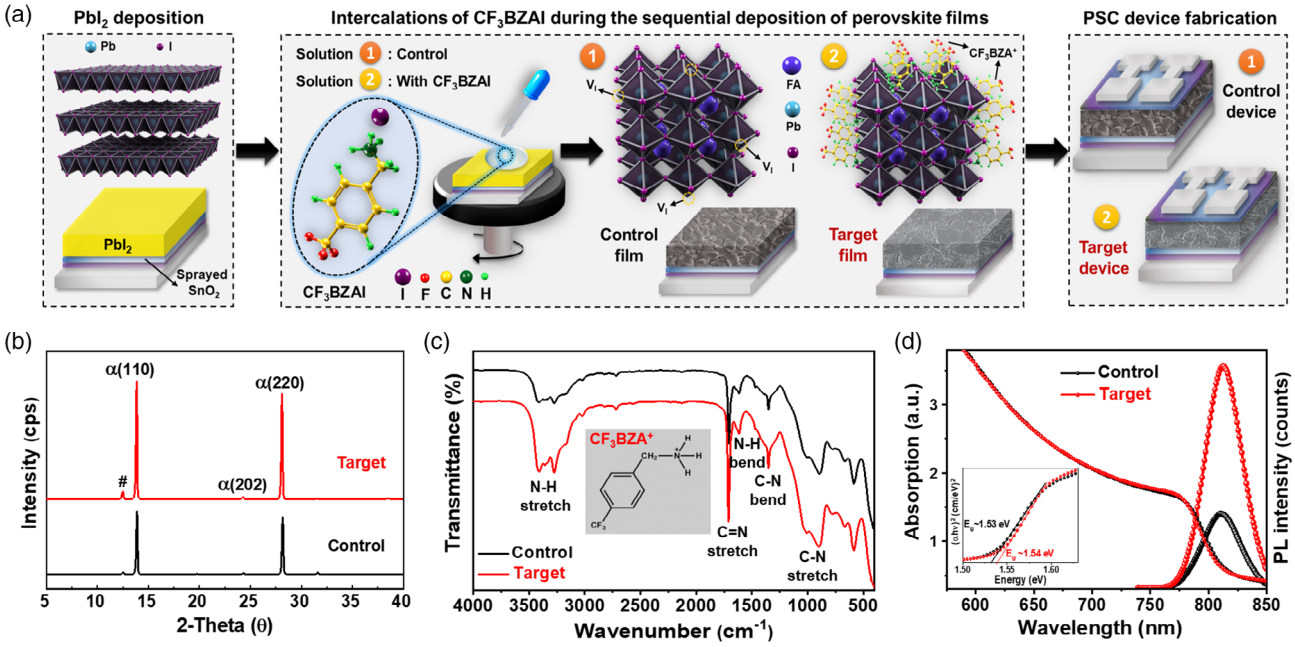

Figure 1. a) Schematic fabrication process of planar PSC devices based on the control and target perovskite films. b) XRD patterns, c) ATR-FTIR spectra; inset shows the molecular structure of CF_3BZA^+, and d) UV–vis absorption and PL spectra of the control and target films.

suggests that there are more radiative emissions in the target film, which can be associated with the reduction of deep trap states in the film. The Tauc plot (inset) shows that the optical bandgap (E_g) of the target film ($E_g \approx 1.54$ eV) is ≈0.01 eV higher than that of the control film ($E_g \approx 1.53$ eV).

The field-emission scanning electron microscope (FESEM) images in **Figure 2**a,b show that both the control and target perovskite films have a highly compact surface filled with humongous grains and distinguishable grain boundaries. The average grain sizes of the control and target perovskite films were measured to be (1.66 ± 0.27) and (1.92 ± 0.23) µm, respectively (Figure S1, Supporting Information), suggesting that the intercalation of a trace amount of CF_3BZAI passivator has led to the growth of bigger grains. As a result of the grain surface

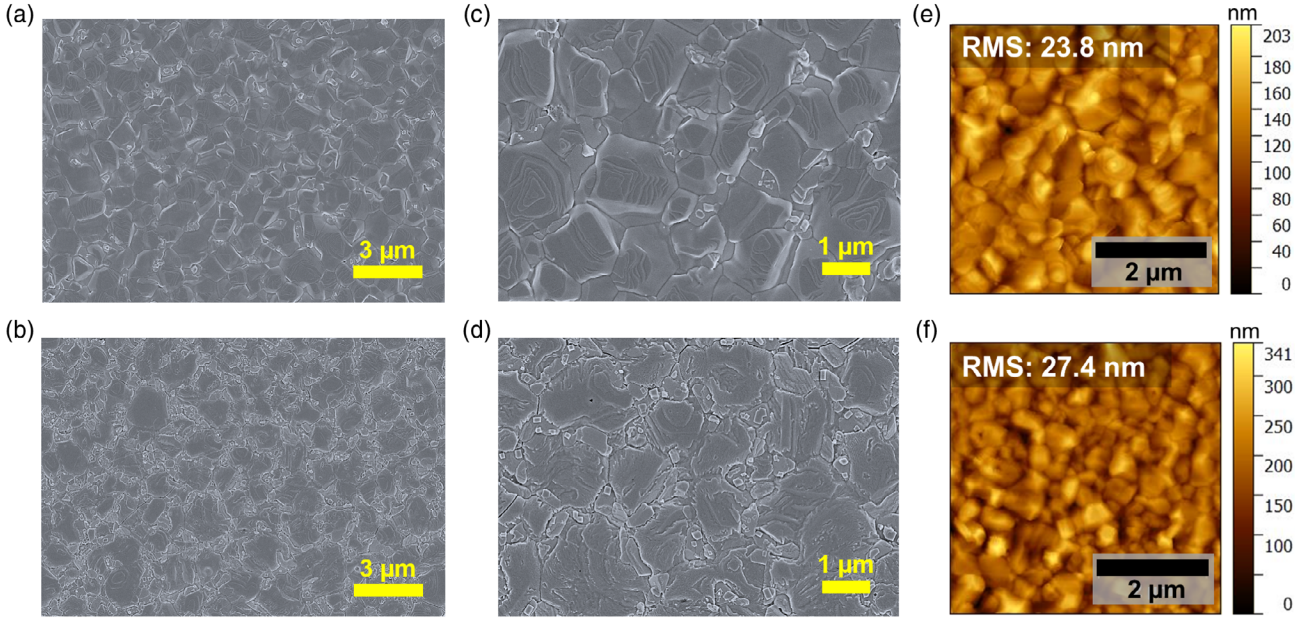

Figure 2. Surface morphology analysis: low-resolution FESEM images of the a) control and b) target perovskite films; high-resolution FESEM images of the c) control and d) target perovskite films. AFM micrographs of the e) control and f) target perovskite films.

passivation effect induced by CF_3BZAI, the target film exhibited a visibly different morphology from that of the control perovskite film. The high-resolution FESEM image in Figure 2c shows that the perovskite grains in the control film have a well-defined hexagonal shape but they are irregular in size. Grain boundaries and protruding PbI_2 grains are clearly visible on the film surface. On the other hand, the intercalation of CF_3BZAI passivator additives seemed to have promoted the growth of nanograins on the surface and along the grain boundaries of the target film (Figure 2d). This created a novel "stitching effect" on the perovskite grains which reduces the grain boundaries in the film. The grain boundary passivation effect observed herein is desirable for perovskite films because grain boundaries are the region where defects are most abundant and charge recombination occurs most frequently. Based on the atomic force microscope (AFM) micrographs of the control (Figure 2e) and target (Figure 2f) perovskite films, the root-mean-square (RMS) roughnesses of the control and target films across a scanned area of $5 \times 5\ \mu m^2$ were measured to be ≈23.8 and ≈27.4 nm, respectively. The increased surface roughness of the target perovskite film is seemingly caused by the presence of nanograins on the surface of the film.

The nanograins anchored on the surface of the target film (resulting from CF_3BZAI intercalation) were further investigated using focused ion beam-transmission electron microscopy (FIB-TEM) measurements. **Figure 3**a displays the cross-sectional FIB-TEM image of the sample with a vertically stacked glass/ITO/SnO_2/perovskite/carbon architecture. The magnified FIB-TEM image in Figure 3a clearly depicts the interface between the ultrathin layer of the nanograins (formed from CF_3BZAI intercalation) and the perovskite film surface. The high-resolution TEM (HRTEM) image in Figure 3b reveals that these newly formed nanograin has lattice fringes with *d*-spacing values of 0.21, 0.22, and 0.32 nm, which can be indexed to the (314), (224), and (220) diffraction planes of cubic perovskite crystal, respectively.[37] This indicates that the nanograins have a 3D cubic perovskite phase. Beneath the film surface, lattice fringes with a *d*-spacing of 0.63 nm corresponding to the main (110) planes of the 3D perovskite were also detected, which is in good agreement with the XRD results. Simultaneously, we also analyzed the region nearby the SnO_2-perovskite interface, and the corresponding low/high magnification FIB-TEM images are displayed in Figure S2, Supporting Information. In the perovskite region, lattice fringes with *d*-spacing values of 0.698 and 0.32 nm corresponding to the PbI_2 (001) and perovskite (211) diffraction planes, respectively, were observed. The selected area electron diffraction patterns in Figure S2, Supporting Information, confirmed the polycrystalline nature of the sample (target perovskite film).

It was previously reported that the bulky CF_3BZA^+ can function as a spacer cation which leads to the formation of low-dimensional crystal phases in perovskite films.[35] However, the HRTEM images show no lattice fringes corresponding to the 2D/quasi-2D layered perovskite phases in the sample, even though 2% of CF_3BZAI passivator additive was introduced during the intercalation process. To further confirm our observation, we performed 2D grazing incidence wide-angle X-ray scattering (GIWAXS) measurements on both the control and target films using an incident angle of 0.2°. The GIWAXS patterns of the control (Figure 3c) and target (Figure 3d) films

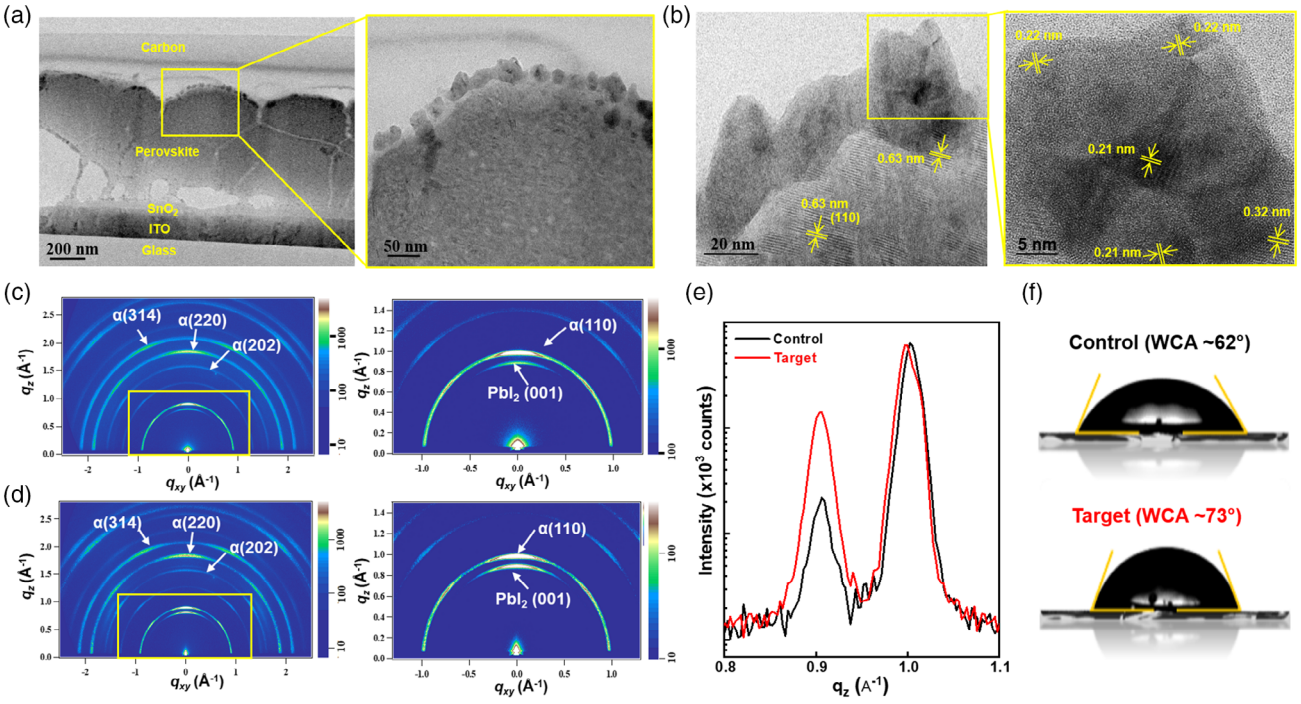

Figure 3. Crystallography analysis of the target film: a) cross-sectional FIB-TEM images showing the nanograins anchored on the top surface of perovskite. b) HRTEM images depicting the lattice fringes found in the nanograins. 2D GIWAXS patterns of the c) control and d) target perovskite films, where the color bars represent the diffraction intensity. e) Diffraction peaks detected along the q_z direction from the 2D GIWAXS images of the perovskite films. Surface wettability analysis: f) WCA profiles of the perovskite films.

are rather similar, in which both exhibited multiple isotropic Bragg rings associated with the (110), (220), (202), and (314) planes of the α-phase (cubic) perovskite. No apparent Bragg spots/marks were observed, indicating that the crystal grains are randomly oriented within the polycrystalline perovskite films.[35] Note that no additional diffraction peaks were observed in the region of $q_{xy} < 1\ \text{Å}^{-1}$ of the target film, confirming the absence of the crystallographic features of the 2D layered structure when intercalating the CF_3BZAI passivators into the inorganic $[PbI_6]^{4-}$ frameworks.[38] This is in good agreement with the HRTEM results. The absence of the 2D perovskite phase following the intercalation of the CF_3BZAI passivators is beneficial for charge transport in the bulk perovskite film. Further magnification of the GIWAXS patterns in the $q_{xy} < 1\ \text{Å}^{-1}$ region provides more information on the Bragg ring arising from the main (110) perovskite phase and the PbI_2 phase in both of the films. The PbI_2 phase is highly textured in the (001) out-of-plane orientation, implying that the PbI_2 phase is probably templated at the buried interfaces of the films.[39] The intensity distribution plots along the q_z direction in Figure 3e reflects stronger detection of the PbI_2 phase in the target film than the control film, which may be due to secondary grain growth (induced by CF_3BZAI passivators) or more severe out-diffusion of the organic cations from the perovskite frameworks during high-temperature (150 °C) annealing.[40,41] Overall, the GIWAXS results are well correlated to the XRD results.

The presence of the CF_3BZAI passivators and nanograins anchored on top of the perovskite surface also altered the wettability of the perovskite film, as revealed by water contact angle (WCA) measurements. Based on the WCA profiles in Figure 3f, it is obvious that the target film (WCA ≈73°) exhibited a more hydrophobic surface than the control film (WCA ≈62°). This is mainly because the surface dispersion force of the target film is retarded by the large steric repulsion in the phenyl ring of the CF_3BZAI molecules, arising from the high electron cloud density surrounding the $-CF_3$ moiety.[15,35] A hydrophobic surface can help to repel moisture and act as a moisture barrier that shields the perovskite film from environmental degradation.

X-ray photoelectron spectroscopy (XPS) measurements were conducted to investigate if the intercalation of CF_3BZAI affected the surface elemental composition of the perovskite films. The XPS survey scan spectra in Figure S3, Supporting Information, show the detection of five primary elements, namely, lead (Pb), iodide (I), bromide (Br), carbon (c), and nitrogen (N) in both the control and target films. In the target film, an additional peak corresponding to fluorine (F) element was

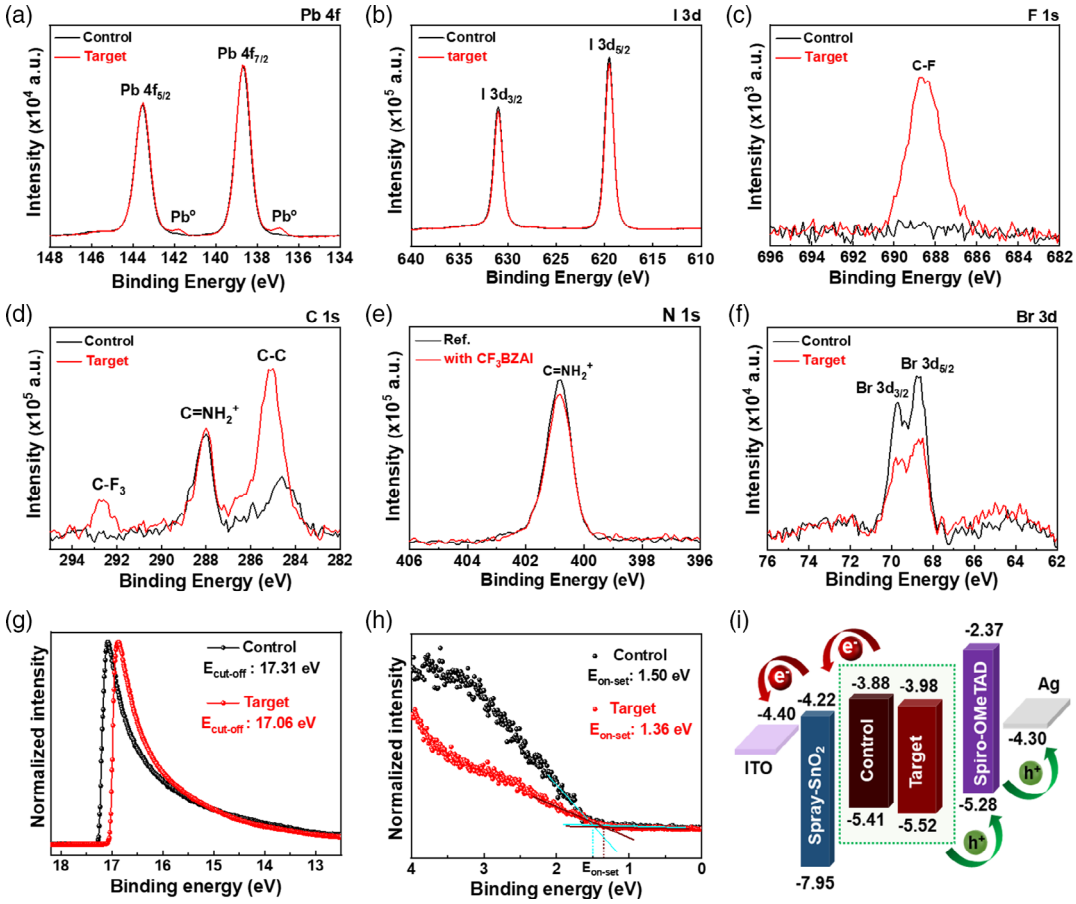

Figure 4. XPS elemental analysis: a) Pb *4f*, b) I *3d*, c) F 1s, d) C 1s, e) N 1s, and f) Br *3d* core-level spectra of the control/target perovskite films. UPS spectra at the g) cutoff region and h) onset region of the perovskite films. i) Schematic energy band level diagram of a PSC device employing control/target perovskite film.

detected. For more in-depth analysis, the core-level spectra of these elements were analyzed. The Pb 4*f* spectra (**Figure 4**a) of both the control and target films consist of two dominant Pb $4f_{5/2}$ and Pb $4f_{7/2}$ peaks at BEs of 143.5 and 138.7 eV, which are commonly associated with the constitutive Pb element in the lattice of the $FAPbI_3$ crystal. The metallic lead (Pb^0) peaks in the target film are marginally higher than the control film, indicating that there is more remnant PbI_2 on the film surface. This finding correlates well with the XRD and GIWAXS data. Meanwhile, there are no significant changes in the I 3*d* (Figure 4b) spectra of the target film compared to the control film, implying that the addition of CF_3BZAI salt has no detrimental effect on the Pb/I stoichiometry of the film. In the F 1*s* spectra (Figure 4c), the target film exhibited a broad C–F peak (BE ≈688.5 eV), which arises from the $–CF_3$ moiety in the phenyl ring of the CF_3BZAI additive. This finding evidences the successful intercalation of CF_3BZAI into the perovskite film. The presence of CF_3BZAI on the surface of the target film can be alternatively confirmed via the detection of the $C–F_3$ peak in the C 1*s* spectra (Figure 4d). Besides the $C–F_3$ peak, the C 1*s* spectra of both perovskite films also contain the signature C–C peak (BE ≈284.6 eV), which arises from the surface adsorbed amorphous carbon, and the $C{=}NH_2^+$ peak (BE ≈287.8 eV) associated with the FA component in the perovskite.[37] In the case of the target film, the increased signal of the C–C peak arose due to the presence of the phenyl group in the CF_3BZA^+cation on the film surface. Similarly, the minor shift of the C–C peak to a higher BE is attributable to the increasing number of highly electronegative fluorine (F) atoms in the CF_3BZA cations which draws electrons from the neighboring carbon atoms. In the N 1*s* spectra (Figure 4e), the detection of the $C{=}NH_2^+$ peak originated mainly from the amino group in the FA^+ cation. The lower intensity of the $C{=}NH_2^+$ peak in the target film can be correlated to the reduced composition ratio (from ≈85% to ≈82%) of FAI salt in the organic solution during the ion intercalation process. Meanwhile, Br element was also detected from both the control and target perovskite films, resulting from extrinsic MABr surface passivation which was performed on both the control and target films to improve their optoelectronic properties (refer Experimental Section). The pronounced broad peaks in the Br 3*d* spectra (Figure 4f) confirmed the successful intercalation of Br ions into the perovskite lattice during the process of MABr surface passivation. The detection of the Br element is noticeably lower in the target film, which is likely due to the presence of intercalated CF_3BZAI passivators that hindered the diffusion of MABr molecules into the perovskite lattice during the passivation treatment.

In conjunction with this analysis, ultraviolet photoelectron spectroscopy (UPS) measurements were conducted to study the effect of CF_3BZAI intercalation on the energy band levels of the control and target perovskite films. Figure 4g,h displays the shifts in the UPS spectra of the perovskite films in the secondary electron cutoff region and valance band region, respectively. Correspondingly, the results revealed an alteration of the E_{cutoff} and E_{onset} parameters of the perovskite film following CF_3BZAI modification. Based on Expression S1, Supporting Information, the highest occupied molecular orbitals (HOMO) levels of the control and target films were determined to be −5.41 and −5.52 eV, respectively. Using the E_g values obtained from the optical absorption data (Figure 1d), the lowest unoccupied molecular orbitals (LUMO) levels of the control and target films were calculated to be −3.88 and −3.98 eV, respectively. The detailed parameters for the UPS analysis are summarized in Table S1, Supporting Information. Based on the obtained parameters, the energy band diagrams of the control and target perovskite films in a PSC device are schematically illustrated in Figure 4i. Although both perovskite films can form a barrier-free band alignment with the commonly used SnO_2 ETL and spiro-MeOTAD HTL in the PSC, the LUMO level of the target film had a reduced energy band offset with the conduction band of the SnO_2 ETL, which could facilitate the extraction of electrons from the perovskite. The target film also has a deeper HOMO level than the control film which could suppress the recombination of charge carriers at the perovskite/HTL interface for better device performance.[37] The XPS and UPS results prove that the intercalation of CF_3BZAI is highly beneficial to the chemical composition and energy band alignment of the perovskite film, which can lead to considerable changes of the device performance of PSCs.

After understanding how the CF_3BZAI additive influences the structural and optoelectronic properties of α-$FAPbI_3$ films, we then investigated the photovoltaic performance of the PSCs devices based on the control perovskite film (control device) and CF_3BZAI-intercalated perovskite film (target device). The planar PSCs fabricated herein have a n–i–p-type architecture of ITO/SnO_2/perovskite/spiro-MeOTAD/Ag, as schematically illustrated in **Figure 5**a. Based on the *J*–*V* curves in Figure 3b, the control device exhibited a PCE of ≈20.7%, combined with a V_{oc} of 1.069 V, a J_{sc} of 23.97 mA cm^{-2}, and a fill factor (FF) of 80.6%. With the use of CF_3BZAI additive, the target device achieved a remarkably higher PCE of ≈22.4%, resulting from the elevated V_{oc} of ≈1.118 V, a J_{sc} of ≈24.32 mA cm^{-2}, and a higher FF of ≈82.2% (**Table 1**). A remarkable ≈8% increment of the PCE was observed for the PSCs following the intercalation of CF_3BZAI. Figure 3b shows that the target device has a correspondingly higher external quantum efficiency (EQE) than the control device. The integrated J_{sc} values derived from the EQE spectra for the control and target devices were ≈23.3 and ≈23.6 mA cm^{-2}, respectively, which correlated well with the measured J_{sc} values (Table 1).

Based on the PCE distribution (in the form of histogram plot) of the PSC devices in Figure 5d, it is clear that the target devices consistently achieved a ≈2% higher PCE than the control devices under the same fabrication conditions. The whisker plots in Figure S4, Supporting Information, reveal that the photovoltaic performances of both the control and target devices were highly reproducible, and the target devices exhibited higher V_{oc}, J_{sc} and FF than the control devices. The enhanced performance of the target device can be primarily attributed to reduced defects at the surface and grain boundaries in the perovskite film following the intercalation of CF_3BZAI. In addition, the target device demonstrated significantly reduced hysteresis (hysteresis index: 0.018) compared to the control device (hysteresis index: 0.029), which can be attributed to the inhibition of ion migration at the defect sites (Figure S5, Supporting Information). In terms of operational stability, the target device clearly showed superior performance compared to the control device. As displayed in Figure 5e, the stabilized current density (J_{stable}, measured at

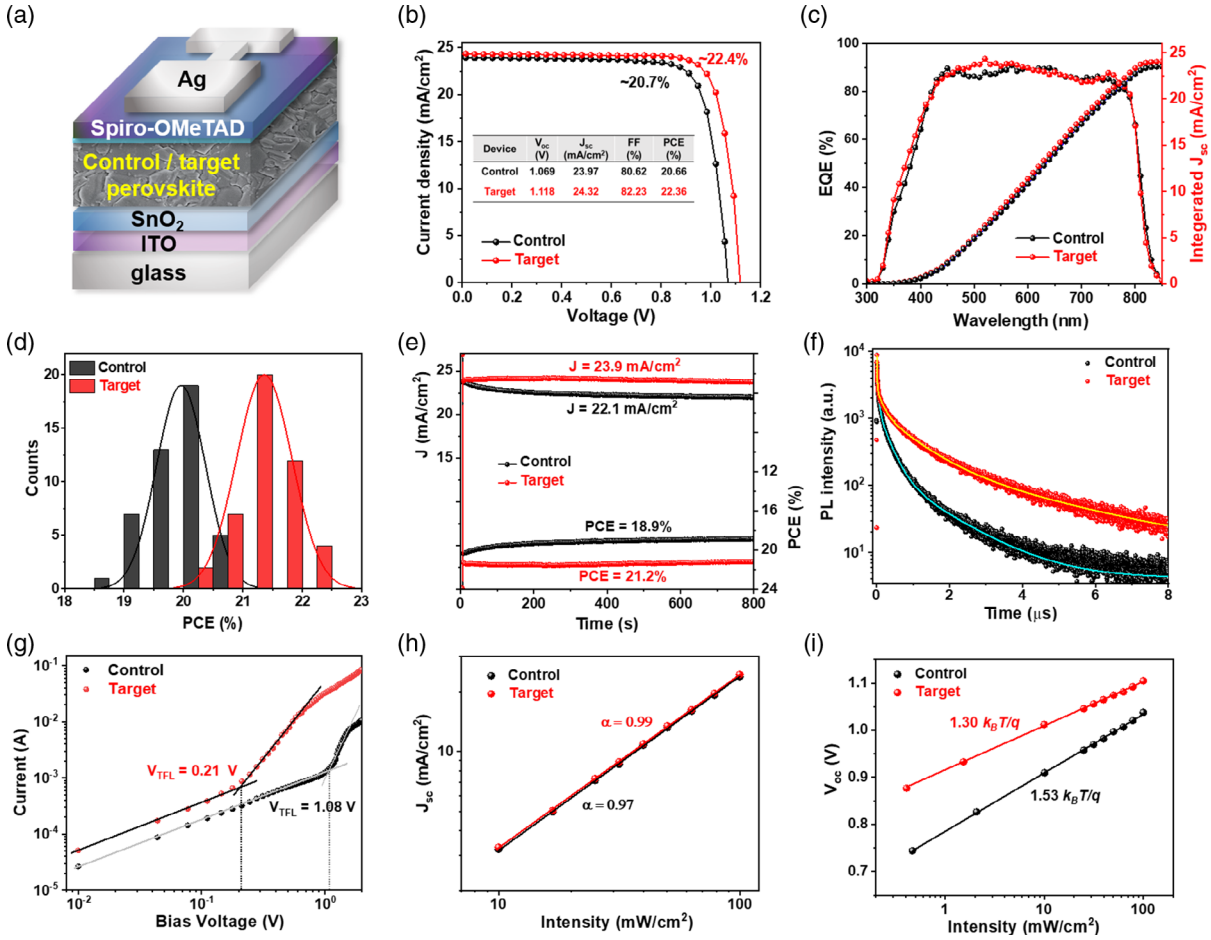

Figure 5. a) Schematic device architecture of planar n–i–p-type PSCs. Device characterization: b) *J–V* curves, c) EQE spectra and integrated J_{sc}, d) PCE histogram plots based on 45 devices, e) stabilized current density and PCE spectra, and f) TRPL spectra of the control and target devices. g) Dark IV plots of electron-only devices based on control and target perovskite films. Response of PSCs under different light intensities: h) J_{sc} and i) V_{oc} versus light intensity plots for the control and target devices.

Table 1. Photovoltaic parameters of the best control and target PSC devices.

Device	Scan directions	V_{oc} [V]	J_{sc} [mA cm^{-2}]	Integrated J_{sc} [mA cm^{-2}]	FF [%]	PCE [%]	PCE_{avg} [%]
Control	Reverse	1.069	23.97	23.28	80.62	20.66	20.37
	Forward	1.051	23.82		80.17	20.07	
Target	Reverse	1.118	24.32	23.64	82.23	22.36	22.16
	Forward	1.106	24.27		81.77	21.95	

the maximum power point) of the control device shows ≈8% deterioration after 800 s of continuous 1 sun illumination, which is commonly known to be caused by halide segregation phenomenon initiated from the ground boundaries of the perovskite film.[42] Meanwhile, there is <2% decrement of the J_{stable} of the target devices under similar conditions. This leads to an increased disparity (≈10%) between the stabilized PCE of the control device ($PCE_{stable} \approx 18.9\%$) and the target device ($PCE_{stable} \approx 21.2\%$).

To determine the reasons behind the improved photovoltaic performance of the PSCs following the intercalation of CF_3BZAI, we thoroughly studied the charge transfer dynamics of the control and target devices. Time-resolved photoluminescence (TRPL) and space-charge-limited-current (SCLC) measurements were performed to provide insights into how the intercalation of CF_3BZAI affects the trap states in the perovskite films. TRPL measurements were conducted on perovskite films in the absence of the electron/hole transport layer to shed light

on the radiative recombination (charge transfer) and nonradiative recombination that occurred in the perovskite films. During the TRPL measurement, the photogenerated charge carriers in the perovskite films can either recombine radiatively to yield PL or be captured by the shallow trap states in the film, leading to nonradiative recombination.[16,43] Figure 5f reveals that the TRPL spectra of the target perovskite film had a significantly slower PL decay than the control perovskite film. In the absence of a charge transporting layer, slower PL decay signifies reduced nonradiative recombination in the perovskite film. The fluorescence lifetime (τ_{PL}) of the perovskite films was then calculated by fitting the TRPL curves with a triexponential decay function (Expression S1, Supporting Information), where the values of the fitting parameters are summarized in Table S2, Supporting Information. Fascinatingly, the τ_{PL} of the perovskite film improved from ≈496 (control) to ≈1622 ns (target) following the intercalation of CF_3BZAI, which is attributable to the significant reduction of deep-level trap states and suppressed nonradiative carrier recombination in the film. The improved τ_{PL} of the target perovskite film correlates well with its higher steady-state PL emission. For SCLC measurements, we fabricated electron-only devices with an architecture of ITO/SnO_2/perovskite/PCBM/Ag and the resulting dark I–V curves of the devices (based on control/target perovskite films) are presented in Figure 5g. In the trap-filling region where the current shows a nonlinear rise, the trap-filled limited voltage (V_{TFL}) of the control$_{SCLC}$ and target$_{SCLC}$ devices were 1.08 and 0.21 V, respectively. Based on the Mott-Gurney relation (Expression S2, Supporting Information), the trap-state densities (N_{trap}) of the control and target devices were calculated to be 7.02×10^{15} and 1.36×10^{15} cm^{-3}, respectively. The reduction of the N_{trap} observed herein agrees well with the TRPL results, showing that the improved performance of the target device originated mainly from the reduction of defects following the intercalation of CF_3BZAI.

Then, we measured the photovoltaic response of the devices under different light intensities. The variations of J_{sc} and V_{oc} under different light intensities are plotted in Figure 5h,i, respectively. Both the control and target devices displayed a linear J_{sc} versus light intensity relationship under short-circuit conditions, indicating that the intercalation of the insulating CF_3BZAI did not induce a charge transport barrier in the perovskite film. On the other hand, the target device showed a smaller slope of $1.30\,k_BT/q$ than the control device ($1.53\,k_BT/q$), where k_B is the Boltzmann constant, T is temperature, and q is the electric charge. The deviation of the slope from k_BT/q herein reflects the possibility of the defect-assisted Shockley–Read–Hall (SRH) recombination in the PSC devices at open-circuit conditions.[44] The reduced ideality factor (IF) of the target device (IF = 1.30) compared to the control device (IF = 1.53) confirmed that the intercalation of CF_3BZAI largely suppressed the SRH charge recombination in the perovskite film through grain boundaries passivation.[44,45] Evidently, the superior photovoltaic performance of the target device originated mainly from the reduced trap-assisted recombination in the target film.

Furthermore, we evaluated the effect of CF_3BZAI intercalation on the long-term stability of the PSCs. For stability tests, the Ag top contacts of the PSC devices were replaced with the more air-stable Au top contacts. Figure S6a,b, Supporting Information, displays the PCE variations of the PSC devices stored in ambient air (temperature: 20–25 °C, relative humidity: 30–40%) and in an N_2-filled glove box, respectively. In both cases, the target devices (based on CF_3BZAI-intercalated film) demonstrated higher PCE retention or superior stability than the control devices. The environmental stability of the PSCs is known to be closely associated with the structural disorders, grain boundaries, and point defects (vacancies or interstitials) in the bulk/surface region of the perovskite film. Grain boundaries, in particular, are prone to moisture ingress and halide segregation because they accommodate the most defects. Through the intercalation of CF_3BZAI passivators, the bulk defects and grain boundaries in the perovskite film reduced substantially, hindering the degradation of the perovskite film under ambient atmosphere. Additionally, the intercalation of CF_3BZAI also boosted the hydrophobicity of the perovskite film surface, effectively blocking the permeation of oxygen and moisture from the surroundings into the perovskite film.[15] When placed in the glovebox, the target devices also showed much slower degradation than the control devices, which is understandably due to the mitigated internal ion migration and halide segregation phenomena within the perovskite film.[46,47] As a result, substantial improvements were observed in both the photovoltaic performance and stability of the CF_3BZAI-intercalated devices.

3. Conclusion

In this study, we fabricated $FAPbI_3$ perovskite films using a two-step sequential deposition technique and intercalated CF_3BZAI as a novel passivator additive. Compared to the normal $FAPbI_3$ (control) film, the CF_3BZAI-intercalated (target) film exhibited enhanced morphology and crystallinity. The target film also contained significantly fewer defects due to the grain surface passivation effect induced by CF_3BZAI. Interestingly, FIB-TEM and GIWAXS measurements confirmed that the intercalation of CF_3BZAI does not lead to the formation of low-dimensional perovskite or impurity phases in the film. In addition, XPS measurements evidenced the successful intercalation of CF_3BZAI into the perovskite framework. The strong steric repulsion in the CF_3BZAI passivator also increased the surface hydrophobicity of the perovskite film, which can enhance the moisture resistance of the film. On the device level, the best PSC device based on the target film (target device) achieved a maximum PCE of ≈22.4%, which is much higher than the control device (PCE ≈20.7%). The improved photovoltaic performance of the PSCs is mainly attributable to the reduced trap states and the suppression of defect-assisted recombination in the perovskite film as a result of CF_3BZAI intercalation. The target device also demonstrated improved operational stability and a more ideal light intensity versus V_{oc} relationship, which are of great importance for the future commercialization of PSCs. Overall, the novel grain surface passivation induced by the intercalation of CF_3BZAI was proven to be highly beneficial for the performance enhancement of PSCs.

4. Experimental Section

Materials: A SnO_2 colloidal dispersion (15 wt% in H_2O) was purchased from Fisher Scientific Korea Ltd., South Korea. Lead (II) iodide

(PbI_2, 99.99%) was purchased from Tokyo Chemical Industry Ltd., Japan. Formamidinium iodide (FAI, >98%), methylammonium iodide (MAI, >99.99%), methylammonium bromide (MABr, >99.99%), methylammonium chloride (MACl, >99.99%), and FK209 cobalt (III) TFSI salt were purchased from Greatcell Solar Materials, Australia. Bis(trifluoromethane) sulfonimide lithium salt (Li-TSFI, 99.95%), 4-*tert*-butylpyridine (4-*t*BP, 96%), dimethylformamide (DMF, anhydrous 99.8%), dimethyl sulfoxide (DMSO, anhydrous >99.9%), 2-propanol, (IPA, anhydrous 99.5%), ethyl acetate (EA, anhydrous 99.5%), hexane (Hex, anhydrous 99.5%), chlorobenzene (anhydrous 99.8%), and acetonitrile (anhydrous 99.8%) were purchased from Sigma-Aldrich. 2,2',7,7'-Tetrakis[*N*,*N*-di(4-methoxyphenyl) amino]-9,9'-spirobifluorene (Spiro-MeOTAD, >99%) was purchased from Luminescence Technology Corporation, Taiwan. All of the materials were used as received without further purification.

PSC Device Fabrication: First, 2.5 cm × 2.5 cm patterned glass/ITO substrates (sheet resistance $\approx 7\ \Omega\ sq^{-1}$) were cleaned via sequential sonication in acetone, ethanol, and isopropyl alcohol. After drying, the substrates were treated by UV-ozone for 15 min to improve surface wettability. A spray solution was prepared by diluting 120 µL of the as-bought SnO_2 colloidal solution in a mixture of 5 mL of deionized (DI) water and 5 mL of methanol. The concentration of colloidal SnO_2 was held at 1.8 mg mL^{-1} for all experiments. The SnO_2 solution was first filtered through a polypropylene filter (0.45 um) and then spray-coated onto the ITO substrates at room temperature using a recipe similar to that reported in our previous work.[37] The SnO_2 films were postannealed at 150 °C for 30 min in ambient air. A perovskite absorber film was prepared via a two-step sequential deposition technique, as demonstrated in our previous work, with some modifications.[37] In the first step, a 1.5 M PbI_2 stock solution in DMF: DMSO (9:1 v/v) was deposited onto ITO/SnO_2 substrates inside an N_2-filled glove box via spincoating at 1500 rpm for 40 s. The PbI_2 film was postbaked at 70 °C for 1 min and cooled down to room temperature. In the second step, the FAI:MAI:MACl (90:9:10 mg mL^{-1} in IPA) or FAI: CF_3BZAI:MAI:MACl (90:4.5:4.5:10 mg mL^{-1} in IPA) solution was spin-coated onto the PbI_2 film at 2200 rpm for 30 s in a glove box. The films were postannealed at 150 °C in ambient air (RH% of 30–45%) for 16 min to convert the PbI_2 film into the perovskite film. For defect passivation, a MABr solution (1.5 mg mL^{-1} in IPA) was spin-casted onto the perovskite films at 4000 rpm for 40 s and postbaked for 120 °C for 10 min to improve the film quality. A spiro-MeOTAD solution was prepared by dissolving 73.2 mg of spiro-MeOTAD salt in 1 mL of chlorobenzene doped with 30 µL of 4-*t*BP, 35 µL of Li-TFSI (260 mg mL^{-1} in acetonitrile), and 28 µL of FK209 (300 mg mL^{-1} in acetonitrile). The spiro-MeOTAD solution was spin-casted onto the perovskite film at 4,000 rpm for 40 s. Finally, ≈120 nm-thick Ag electrodes were thermally evaporated onto the active layers through metal masks with an aperture area of 0.10 cm^2 inside a high-vacuum ($\approx 5 \times 10^{-6}$ Torr) chamber.

Material and Device Characterization: The structural information and crystallographic changes of the perovskite films were studied using an X-ray diffractometer (D8 Advance, Bruker) with Cu Kα excitation. The surface morphology and topography of the perovskite films were examined using a FESEM (SU-70, Hitachi) and an AFM (NX10, Park Systems), respectively. A Cs-corrected, high-angle annular dark-field scanning transmission electron microscope, HAADF-STEM (JEM-ARM200F, JEOL), was used to analyze the nanocrystallography of the perovskite films. For the measurements, the perovskite film was first sputter-coated with carbon and cross-sectionally cut using (FIB) milling. The previously mentioned research facilities are at the Center for University-Wide Research Facilities (CURF) at Jeonbuk National University (JBNU), Korea. Synchrotron radiation GIWAXS measurements were performed using the 5 A beamline with a wavelength of 1.0716 Å at the Pohang Accelerator Laboratory (PLSII, Korea) for in-depth analysis of the perovskite crystal orientations. 2D GIWAXS patterns were acquired at an incident angle (θ_i) of 0.2° using a Mar3450 image detector with a sample-to-detector distance (SDD) of 0.298 m. The optical absorption of the perovskite films was measured using a UV–vis spectrophotometer (Lambda 750, PerkinElmer). Steady-state PL spectra of the perovskite films were acquired using a fluorescence spectrophotometer (FluoroMax-4, Horiba) at an excitation wavelength of 480 nm. The changes of the chemical composition on the surface of the perovskite films were studied via XPS and UPS measurements using a MultiLab 2000 (THERMO VG SCIENCE) with monochromatized Mg Kα radiation at $h\nu = 1253.6$ eV at a base pressure of $\approx 10^{-9}$ Pa (KBSI). TRPL) profiles of the films were acquired from an inverted-type scanning confocal microscope (MicroTime-200, Picoquant, Germany) with a 4× (air) objective using a single-mode 470 nm pulsed laser diode (pulse width of ≈30 ps; average power of ≈100 nW with a 200 kHz repetition rate) as an excitation source. A dichroic mirror (490 DCXR, AHF), a long pass filter (FEL0600, Thorlabs), and a single photon avalanche diode (PDM series, MPD) were used to collect emissions from the samples, where a time-correlated single-photon counting system (TimeHarp-260, PicoQuant GmbH, Germany) was used to count the photon emissions in 5 µs time windows with a time resolution of 1 ns. The exponential fitting for the phosphorescence decay was carried out using Symphotime-64 software (Ver. 2.2). The TRPL setup is installed at the Korea Basic Science Institute (KBSI), Daegu Center, Korea. The *J–V* characteristic curves of the PSC devices were obtained using a Keithley 2400 source meter SMU instrument (Tektronix Inc.) under simulated 1 sun (100 mW cm^{-2}) illumination provided by an Oriel Sol AAA solar simulator equipped with an AM1.5G standard filter (Newport Inc.). The intensity of the illumination was precalibrated using an NREL-certified silicon solar cell prior to conducting the measurements. The EQEs of the devices were determined using a quantum efficiency measurement system (Oriel IQE-200, Newport, Inc.).

Supporting Information

Supporting Information is available from the Wiley Online Library or from the author.

Acknowledgements

H.B.L. and N.K. contributed equally to this work. This work was financially supported by the Basic Science Research Program [NRF-2021R1A2C2004206, NRF-2021R1I1A1A01056643, and NRF-2021R1I1A1A01057909] through the National Research Foundation (NRF) of Korea, funded by the Ministry of Science, ICT & Future Planning.

Conflict of Interest

The authors declare no conflict of interest.

Data Availability Statement

The data that support the findings of this study are available in the supplementary material of this article.

Keywords

crystal growths, defects, grain boundaries, passivator adsorptions, surfaces and interfaces

Received: August 29, 2022
Revised: October 30, 2022
Published online: November 29, 2022

[1] F. Zhang, H. Lu, J. Tong, J. J. Berry, M. C. Beard, K. Zhu, *Energy Environ. Sci.* **2020**, *13*, 1154.
[2] H. B. Lee, N. Kumar, B. Tyagi, S. He, R. Sahani, J.-W. Kang, *Mater. Today Energy* **2021**, *21*, 100759.

[3] H. Chen, Y. Chen, T. Zhang, X. Liu, X. Wang, Y. Zhao, *Small Struct.* **2021**, *2*, 2000130.
[4] E. Aydin, M. Bastiani, S. Wolf, *Adv. Mater.* **2019**, *31*, 1900428.
[5] Y. Li, H. Wu, W. Qi, X. Zhou, J. Li, J. Cheng, Y. Zhao, Y. Li, X. Zhang, *Nano Energy* **2020**, *77*, 105237.
[6] S. Masi, A. F. Gualdrón-Reyes, I. Mora-Seró, *ACS Energy Lett.* **2020**, *5*, 1974.
[7] H. B. Lee, M. Jeon, N. Kumar, B. Tyagi, J. Kang, *Adv. Funct. Mater.* **2019**, *29*, 1903213.
[8] X. Cao, L. Hao, Z. Liu, G. Su, X. He, Q. Zeng, J. Wei, *Chem. Eng. J.* **2022**, *437*, 135458.
[9] B. Tyagi, H. B. Lee, N. Kumar, J.-W. Kang, *ACS Appl. Energy Mater.* **2020**, *3*, 8595.
[10] I. S. Yang, N. Park, *Adv. Funct. Mater.* **2021**, *31*, 2100396.
[11] J. Zhang, L. Wang, C. Jiang, B. Cheng, T. Chen, J. Yu, *Adv. Sci.* **2021**, *8*, 2102648.
[12] H. Bi, B. Liu, D. He, L. Bai, W. Wang, Z. Zang, J. Chen, *Chem. Eng. J.* **2021**, *418*, 129375.
[13] M. Lyu, N.-G. Park, *Sol. RRL* **2020**, *4*, 2000331.
[14] C. Li, A. Wang, L. Xie, X. Deng, K. Liao, J. Yang, T. Li, F. Hao, *J. Mater. Chem. A* **2019**, *7*, 24150.
[15] H. B. Lee, N. Kumar, V. Devaraj, B. Tyagi, S. He, R. Sahani, K.-J. Ko, J.-W. Oh, J.-W. Kang, *Sol. RRL* **2021**, *5*, 2100712.
[16] H. B. Lee, N. Kumar, B. Tyagi, K.-J. Ko, J.-W. Kang, *Sol. RRL* **2021**, *5*, 2000589.
[17] R. Lin, J. Xu, M. Wei, Y. Wang, Z. Qin, Z. Liu, J. Wu, K. Xiao, B. Chen, S. M. Park, G. Chen, H. R. Atapattu, K. R. Graham, J. Xu, J. Zhu, L. Li, C. Zhang, E. H. Sargent, H. Tan, *Nature* **2022**, *603*, 73.
[18] S. Gharibzadeh, P. Fassl, I. M. Hossain, P. Rohrbeck, M. Frericks, M. Schmidt, T. Duong, M. R. Khan, T. Abzieher, B. A. Nejand, F. Schackmar, O. Almora, T. Feeney, R. Singh, D. Fuchs, U. Lemmer, J. P. Hofmann, S. A. L. Weber, U. W. Paetzold, *Energy Environ. Sci.* **2021**, *14*, 5875.
[19] C. Zhang, W. Kong, T. Wu, X. Lin, Y. Wu, J. Nakazaki, H. Segawa, X. Yang, Y. Zhang, Y. Wang, L. Han, *ACS Appl. Mater. Interfaces* **2021**, *13*, 44321.
[20] H. Su, X. Lin, Y. Wang, X. Liu, Z. Qin, Q. Shi, Q. Han, Y. Zhang, L. Han, *Sci. China Chem.* **2022**, *65*, 1321.
[21] F. Ye, J. Ma, C. Chen, H. Wang, Y. Xu, S. Zhang, T. Wang, C. Tao, G. Fang, *Adv. Mater.* **2021**, *33*, 2007126.
[22] L. Su, Y. Xiao, G. Han, L. Lu, H. Li, M. Zhu, *J. Power Sources* **2019**, *426*, 11.
[23] I. M. Asuo, I. Ka, D. Gedamu, A. Pignolet, R. Nechache, S. G. Cloutier, *Sol. Energy Mater. Sol. Cells* **2019**, *200*, 110029.
[24] T. Liu, H. Lai, X. Wan, X. Zhang, Y. Liu, Y. Chen, *Chem. Mater.* **2018**, *30*, 5264.
[25] J. Zhang, T. Bu, J. Li, H. Li, Y. Mo, Z. Wu, Y. Liu, X.-L. Zhang, Y.-B. Cheng, F. Huang, *J. Mater. Chem. A* **2020**, *8*, 8447.
[26] Z. Xiong, X. Chen, B. Zhang, G. O. Odunmbaku, Z. Ou, B. Guo, K. Yang, Z. Kan, S. Lu, S. Chen, N. A. N. Ouedraogo, Y. Cho, C. Yang, J. Chen, K. Sun, *Adv. Mater.* **2022**, *34*, 2106118.
[27] Y. Wang, H. Xu, F. Wang, D. Liu, H. Chen, H. Zheng, L. Ji, P. Zhang, T. Zhang, Z. D. Chen, J. Wu, L. Chen, S. Li, *Chem. Eng. J.* **2020**, *391*, 123589.
[28] N. Mozaffari, T. Duong, M. M. Shehata, A. D. Bui, H. T. Pham, Y. Yin, Y. O. Mayon, J. Zheng, M. A. Mahmud, G. D. Tabi, G. G. Andersson, L. E. Black, J. Peng, H. Shen, T. P. White, K. Weber, K. R. Catchpole, *Sol. RRL* **2022**, *6*, 2200355.
[29] Q. Jiang, Y. Zhao, X. Zhang, X. Yang, Y. Chen, Z. Chu, Q. Ye, X. Li, Z. Yin, J. You, *Nat. Photonics* **2019**, *13*, 460.
[30] J. Wang, L. Liu, S. Chen, L. Qi, M. Zhao, C. Zhao, J. Tang, X. Cai, F. Lu, T. Jiu, *Small* **2022**, *18*, 2104100.
[31] R. Yang, R. Li, Y. Cao, Y. Wei, Y. Miao, W. L. Tan, X. Jiao, H. Chen, L. Zhang, Q. Chen, H. Zhang, W. Zou, Y. Wang, M. Yang, C. Yi, N. Wang, F. Gao, C. R. McNeill, T. Qin, J. Wang, W. Huang, *Adv. Mater.* **2018**, *30*, 1804771.
[32] H. Ren, S. Yu, L. Chao, Y. Xia, Y. Sun, S. Zuo, F. Li, T. Niu, Y. Yang, H. Ju, B. Li, H. Du, X. Gao, J. Zhang, J. Wang, L. Zhang, Y. Chen, W. Huang, *Nat. Photonics* **2020**, *14*, 154.
[33] A. H. Proppe, A. Johnston, S. Teale, A. Mahata, R. Quintero-Bermudez, E. H. Jung, L. Grater, T. Cui, T. Filleter, C.-Y. Kim, S. O. Kelley, F. De Angelis, E. H. Sargent, *Nat. Commun.* **2021**, *12*, 3472.
[34] Y. Zhang, J. Chen, X. Lian, M. Qin, J. Li, T. R. Andersen, X. Lu, G. Wu, H. Li, H. Chen, *Small Methods* **2019**, *3*, 1900375.
[35] J. Li, T. Bu, Z. Lin, Y. Mo, N. Chai, X. Gao, M. Ji, X.-L. Zhang, Y.-B. Cheng, F. Huang, *Chem. Eng. J.* **2021**, *405*, 126712.
[36] H. Lai, D. Lu, Z. Xu, N. Zheng, Z. Xie, Y. Liu, *Adv. Mater.* **2020**, *32*, 2001470.
[37] N. Kumar, H. B. Lee, R. Sahani, B. Tyagi, S. Cho, J. Lee, J. Kang, *Small Methods* **2022**, *6*, 2101127.
[38] P. Cheng, P. Wang, Z. Xu, X. Jia, Q. Wei, N. Yuan, J. Ding, R. Li, G. Zhao, Y. Cheng, K. Zhao, S. F. Liu, *ACS Energy Lett.* **2019**, *4*, 1830.
[39] E. Ugur, A. D. Sheikh, R. Munir, J. I. Khan, D. Barrit, A. Amassian, F. Laquai, *ACS Energy Lett.* **2017**, *2*, 1960.
[40] L. Liu, Y. Bai, X. Zhang, Y. Shang, C. Wang, H. Wang, C. Zhu, C. Hu, J. Wu, H. Zhou, Y. Li, S. Yang, Z. Ning, Q. Chen, *Angew. Chemie* **2020**, *132*, 6035.
[41] C. Ji, C. Liang, H. Zhang, M. Sun, Q. Song, F. Sun, X. Feng, N. Liu, H. Gong, D. Li, F. You, Z. He, *ACS Appl. Mater. Interfaces* **2020**, *12*, 20026.
[42] Y. Zhao, P. Miao, J. Elia, H. Hu, X. Wang, T. Heumueller, Y. Hou, G. J. Matt, A. Osvet, Y.-T. Chen, M. Tarragó, D. de Ligny, T. Przybilla, P. Denninger, J. Will, J. Zhang, X. Tang, N. Li, C. He, A. Pan, A. J. Meixner, E. Spiecker, D. Zhang, C. J. Brabec, *Nat. Commun.* **2020**, *11*, 6328.
[43] H. Zhu, Y. Ren, L. Pan, O. Ouellette, F. T. Eickemeyer, Y. Wu, X. Li, S. Wang, H. Liu, X. Dong, S. M. Zakeeruddin, Y. Liu, A. Hagfeldt, M. Grätzel, *J. Am. Chem. Soc.* **2021**, *143*, 3231.
[44] Y. Luan, F. Wang, J. Zhuang, T. Lin, Y. Wei, N. Chen, Y. Zhang, F. Wang, P. Yu, L. Mao, H. Liu, J. Wang, *EcoMat* **2021**, *3*, e12092.
[45] G. Wu, X. Li, J. Zhou, J. Zhang, X. Zhang, X. Leng, P. Wang, M. Chen, D. Zhang, K. Zhao, S. Liu, H. Zhou, Y. Zhang, *Adv. Mater.* **2019**, *31*, 1903889.
[46] S. Tan, I. Yavuz, N. De Marco, T. Huang, S. Lee, C. S. Choi, M. Wang, S. Nuryyeva, R. Wang, Y. Zhao, H. Wang, T. Han, B. Dunn, Y. Huang, J. Lee, Y. Yang, *Adv. Mater.* **2020**, *32*, 1906995.
[47] E. Bi, Z. Song, C. Li, Z. Wu, Y. Yan, *Trends Chem.* **2021**, *3*, 575.